1996

Pressure dependence and metastable state formation in the photolysis of dichlorine monoxide (Cl2O)

Scott L. Nickolaisen

Charles E. Miller
Haverford College

Stanley P. Sander

Michael R. Hand

Pressure dependence and metastable state formation in the photolysis of dichlorine monoxide (Cl2O)

Scott L. Nickolaisen, Charles E. Miller, Stanley P. Sander, Michael R. Hand, Ian H. Williams et al.

Citation: J. Chem. Phys. **104**, 2857 (1996); doi: 10.1063/1.471109
View online: http://dx.doi.org/10.1063/1.471109
View Table of Contents: http://jcp.aip.org/resource/1/JCPSA6/v104/i8
Published by the American Institute of Physics.

Pressure dependence and metastable state formation in the photolysis of dichlorine monoxide (Cl_2O)

Scott L. Nickolaisen,[a] Charles E. Miller, and Stanley P. Sander[b]
Jet Propulsion Laboratory, California Institute of Technology, 4800 Oak Grove Drive, Pasadena, California 91109

Michael R. Hand and Ian H. Williams
School of Chemistry, University of Bath, Claverton Down, Bath BA2 7AY, United Kingdom

Joseph S. Francisco
Department of Chemistry, Purdue University, W. Lafayette, Indiana 47907-1397

(Received 25 July 1995; accepted 15 November 1995)

The photodissociation of dichlorine monoxide (Cl_2O) was studied using broadband flash photolysis to investigate the influence of variations in the photolysis wavelength domain, bath gas pressure and bath gas identity on the yield and temporal dependence of the ClO product. ClO yields were independent of bath gas pressure when the photolysis spectral band extended to 200 nm (quartz cutoff) but for photolysis restricted to wavelengths longer than about 250 nm, ClO yields decreased with increasing bath gas pressure and there was a pressure-dependent delay in the formation of ClO. Under these conditions, a weak, highly structured absorption spectrum was observed in the range 16 600–26 000 cm^{-1} with a lifetime on the order of 500 ms. A portion of the spectrum could be analyzed (22 000–26 000 cm^{-1}) which showed progressions having differences of 283, 443, and 505 cm^{-1}. *Ab initio* calculations were performed to evaluate vertical excitation energies and oscillator strengths from the lowest-energy singlet ($X\ ^1A_1$) or triplet ($1\ ^3B_1$) states to various excited states. The calculations indicated that the $2\ ^3A_2 \leftarrow 1\ ^3B_1$ transition has an unusually large oscillator strength. The transition energy, 3.05 eV, is consistent with the observed metastable spectrum. The observed pressure dependence of ClO formation could be modeled using a mechanism which assumed that Cl_2O excitation at wavelengths longer than about 300 nm leads to rapid intersystem crossing to two metastable states in the triplet manifold. These states undergo competitive dissociation to ClO+Cl and collisional relaxation to the ground state. The dynamics of Cl_2O may serve as a model for other molecules of importance in the earth's lower stratosphere such as $ClONO_2$ where filtering of the solar spectrum by ozone restricts photolysis to the weak tail of the absorption continuum. © *1996 American Institute of Physics.* [S0021-9606(96)01608-3]

I. INTRODUCTION

The photodissociation of chlorine oxides has received considerable attention in recent years due to their involvement in stratospheric ozone depletion by chlorofluorocarbons. Cl_2O (chlorine monoxide or dichlorine monoxide) is the anhydride of an important chlorine reservoir species in the stratosphere, HOCl, but does not itself play a significant role in atmospheric chemistry. There is, however, interest in understanding the kinetics and photodissociation of Cl_2O. Because it is used extensively as a ClO source through direct photolysis,

$$Cl_2O + h\nu \rightarrow ClO + Cl \quad \lambda_{thresh} = 840 \text{ nm}$$

and by the rapid reaction with atomic chlorine,

$$Cl_2 + h\nu \rightarrow 2Cl,$$

$$Cl + Cl_2O \rightarrow ClO + Cl_2,$$

it is important to quantify the wavelength dependences of the overall quantum yields for all photolytic channels.

Early studies of Cl_2O photodissociation showed that irradiation at wavelengths below 300 nm leads primarily to formation of ClO+Cl, with minor channels leading to $O(^3P)$ or $O(^1D)$ by the reactions

$$Cl_2O + h\nu \rightarrow 2Cl + O(^3P) \quad \lambda_{thresh} = 292 \text{ nm},$$

$$Cl_2O + h\nu \rightarrow Cl_2 + O(^3P) \quad \lambda_{thresh} = 710 \text{ nm},$$

$$Cl_2O + h\nu \rightarrow Cl_2 + O(^1D) \quad \lambda_{thresh} = 335 \text{ nm}.$$

Finkelnburg *et al.* and Schumacher and Townend used steady-state photolysis sources combined with measurements of the Cl_2 quantum yield to deduce the primary quantum yields.[1,2] Later flash photolysis studies of Cl_2O employed the direct detection of ClO.[3,4] Sander and Friedl[5] observed the formation of BrO in the broadband photolysis of Cl_2O–Br_2 systems at wavelengths longer than 180 nm. In this experiment, the only likely pathway for the formation of BrO was the $O(^3P) + Br_2$ reaction, with the $O(^3P)$ being produced by Cl_2O photolysis. The measured $O(^3P)$ quantum yield over the photolysis band was 25%±5%. Recently, Nelson *et al.*[6] have employed photofragment translational energy spectros-

[a]Permanent address: Department of Chemistry and Biochemistry, California State University, Los Angeles, 5151 State University Drive, Los Angeles, CA 90032.
[b]Author to whom correspondence should be addressed.

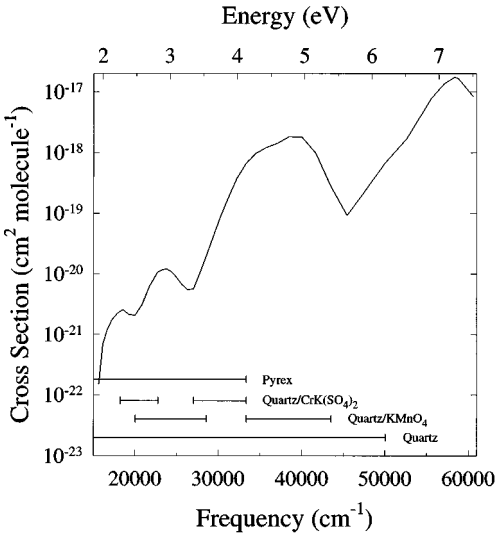

FIG. 1. Cl_2O absorption cross sections vs wavelength. Bars indicate excitation regions for photolysis cell/filter solution combinations discussed in the text.

copy in a molecular beam to study Cl_2O photodissociation mechanisms at 308, 248, and 193 nm. This work showed that primary Cl–O bond fission occurs at all three wavelengths. At 248 and 193 nm the ClO fragment possessed sufficient internal energy to undergo secondary dissociation and at 193 nm there was evidence for concerted Cl_2 elimination pathways on both the singlet and triplet surfaces. While this experiment provided considerable information on the dynamics of the primary and secondary reaction channels, it did not probe the photolysis in the weak tail of the Cl_2O absorption continuum beyond 308 nm or effects due to collisions. Chichinin[7] studied the 248 nm photolysis of Cl_2O using time resolved laser magnetic resonance to measure the extent of spin–orbit excitation of nascent $Cl(^2P_J)$. The atomic chlorine was found to be predominantly (82%) in the ground $(^2P_{3/2})$ state at this wavelength but quantum yields at longer wavelengths and the effect of buffer gas collisions were not examined.

Cl_2O is characterized by a continuous absorption spectrum with maxima at 530, 410, 256, and 171 nm, and a vibrationally resolved Rydberg series with an absorption maximum at 161.1 nm (Fig. 1).[8–11] The electronic states responsible for the observed ultraviolet absorption bands have not been determined experimentally or theoretically. Because the Cl_2O absorption cross sections decrease rapidly to values less than 10^{-20} molecule cm^{-2} beyond 350 nm direct probing of the photodissociation dynamics of the visible band systems is quite difficult due to the small fractional decomposition of the photolyte.

Photodissociation in the weak absorption tail is a problem that is very important for stratospheric and tropospheric chemistry. Species that are important temporary reservoirs of odd hydrogen, nitrogen, chlorine, and bromine such as $ClONO_2$ and $HONO_2$ are most abundant in the lower stratosphere below 30 km. In this region of the atmosphere, ozone absorption removes virtually all solar radiation below 290 nm. At wavelengths longer than this cutoff point, the absorption cross sections of many temporary reservoir species are small due to weak Franck–Condon overlap or forbidden electronic transitions. Nevertheless, photolysis is the most important loss process for these molecules in the lower stratosphere. Results of photodissociation studies carried out at shorter wavelengths, or under different conditions of temperature and pressure than those encountered in the lower stratosphere may not be applicable to the real atmosphere. Errors in the measurement of effective quantum yields will have a significant impact on the ability of atmospheric models to correctly predict the abundance and partitioning of trace species, and therefore affect calculations of stratospheric ozone loss. As indicated above, while Cl_2O is not a molecule that is directly relevant to atmospheric chemistry, studies of its photodissociation at long wavelengths may serve as a paradigm for the understanding of the photolysis of stratospheric temporary reservoir species.

One approach to the investigation of photolysis processes in weakly absorbing bands is to use a broadband photolysis source such as a flashlamp coupled with analysis by time-resolved absorption spectroscopy. While a flashlamp lacks the wavelength specificity to initiate photolysis from a well-defined initial state, it can provide a large photolysis flux in the region of low absorption cross section of the photolyte. We have used this approach to study the photolysis of Cl_2O. Photolysis filters were used to isolate photolysis spectral regions from 180 nm through the visible. The yields and time-dependent concentrations of ClO were measured as a function of buffer gas density using an optical multichannel analyzer (OMA). The spectrum of a new intermediate was identified in the photolysis of Cl_2O at wavelengths longer than 300 nm. *Ab initio* calculations have been carried out to determine the energy ordering and oscillator strengths for transitions in the singlet and triplet manifolds of Cl_2O using the complete-active-space self-consistent-field (CASSCF) and multireference configuration-interaction (MRCI) methods for the singlet and triplet ground and excited states, respectively.

II. EXPERIMENT

Cl_2O was prepared by the method of Cady[12] in which a mixture of 10%–20% Cl_2 in helium was slowly flowed over dried HgO at room temperature and at a total pressure of 250 Torr. The effluent gas was collected in a trap at 161 K. Cl_2O was purified of residual Cl_2 by vacuum distillation at 196 K. The purity of the sample was checked by uv absorption spectroscopy. The only detectable impurity was OClO at 0.2 pptv with no discernible Cl_2 impurity. Cl_2O was introduced into the flash photolysis apparatus by flowing UHP helium (Matheson) through the liquid sample at 196 K. The helium pressure in the sample bubbler was varied from 500–1020 Torr depending on the desired concentration of Cl_2O and flow rate within the reaction cell.

The flash photolysis apparatus employed has been used in this laboratory for many studies and is described in detail elsewhere.[5] A brief outline of the features important for these

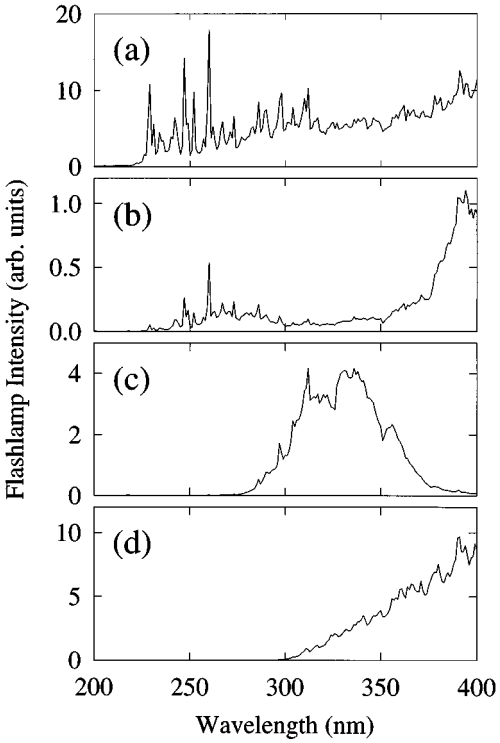

FIG. 2. Flashlamp spectral distributions for different photolysis cell/filter combinations: (a) unfiltered quartz cell; (b) quartz cell with $KMnO_4$ (0.2 g L^{-1}) filter solution; (c) quartz cell with $CrK(SO_4)_2 \cdot 12H_2O$ (100 g L^{-1}) filter solution; (d) unfiltered Pyrex cell.

experiments follows. Identical reaction cells fabricated from Pyrex or quartz were used in these experiments, depending on the range of photolysis wavelengths desired. Each cell consisted of a central reaction region 90.5 cm in length through which the gas mixture flowed. The reaction cell was surrounded by three annular jackets. The innermost jacket comprised an optical filter into which inorganic salt solutions could be added to provide coarse wavelength filtering of the spectral distribution of the photolyzing light. The middle jacket comprised a flashlamp which was used to initiate photodissociation of chlorine oxide. This jacket was filled with 30–50 Torr xenon which was discharged with a 27.5 kV potential through a 2.4 μF capacitor to produce a high intensity broadband flash. The outermost jacket was connected to a heater/chiller to provide temperature control of the reactor contents.

The two different cell provided some wavelength control of the photolysis light—the Pyrex cell cuts off wavelengths shorter than 300 nm due to the intrinsic properties of the material, and the quartz cell extended the photolysis cut off to 200 nm. Spectral distributions of the photolysis flash with each filter and cell were obtained by recording the spectral distribution of the photolysis light scattered along the probe beam detection axis. The associated spectral distributions from 200 to 400 nm are shown in Figs. 2(a)–2(d). To further limit the spectral distribution of the flashlamp, two salt solutions were used. A solution of $KMnO_4$ (0.2 g L^{-1}) provided a weak transmission band between 230 and 300 nm with greater transmission between 350 and 500 nm [Fig. 2(b)]. A solution of $CrK(SO_4)_2 \cdot 12H_2O$ (100 g L^{-1}) had banded transmission between 285–375 and 440–550 nm [Fig. 2(c)].

A. ClO product yield and temporal behavior

Time-dependent concentrations of reactants and products were measured by long-path uv absorption spectroscopy. The collimated output of a 150 W short arc xenon lamp was passed through the reaction cell using White-type optics to provide a total optical path length of 724 cm. The beam was passed to a 0.3 m monochromator equipped with a 1024 pixel diode array detector. A 2400 line mm^{-1} diffraction grating was used which, when coupled with the diode array detector, resulted in the detection of a spectral band of 30 nm width. With this detection scheme, the prominent ClO vibrational progression of the $\Omega=3/2$ subband ($A \leftarrow X$) transition in the region 265–295 nm could be seen in a single scan of the detector array. By using dedicated memory locations for data storage, the diode array control electronics and interface allowed for the acquisition of up to 512 separate scans of the detector array for each firing of the flashlamp. The temporal resolution of the experiments was determined by the number of pixels read in each scan—when the entire 1024 pixels were read, the minimum temporal resolution was 16.67 ms, but this value could be reduced to 5 ms when a subset of only 270 adjacent pixels were used. This lower value resulted from the minimum number of pixels needed in order to maintain the unambiguous detection of ClO by the observation of at least five of the vibrational bands centered at 275 nm. Temporal information on the formation and subsequent removal of the ClO product was obtained by averaging 5 to 100 transient absorption signals following firing of the flashlamp and fitting the spectra resulting from each scan of the detector array to a reference spectrum determined from the known relative cross sections of ClO.[13] While absolute ClO cross sections are dependent on spectrometer resolution, the measurements here were carried out using the same optical configuration as those employed by Nickolaisen *et al.* in which absolute and relative ClO cross sections were measured with estimated uncertainties of $\pm 20\%$ and $\pm 5\%$, respectively.

The ClO product yield as a function of total pressure was measured under conditions of constant Cl_2O concentration. Total flow of the gas mixture through the cell was adjusted so that the residence time within the cell was always 5–10 s shorter than the duty cycle of the flashlamp ensuring that all photolysis and reaction products are flushed from the cell between each firing of the flashlamp.

B. Absorption spectra of intermediates

For detection of absorption spectra of possible intermediates resulting from Cl_2O photolysis, a method was used that was similar to the one described above with certain modifications. The monochromator was fitted with a 1200 line mm^{-1} diffraction resulting in a spectral bandwidth of 60 nm. Because of the very small absorption signals involved in these measurements, it was necessary to perform 100 coad-

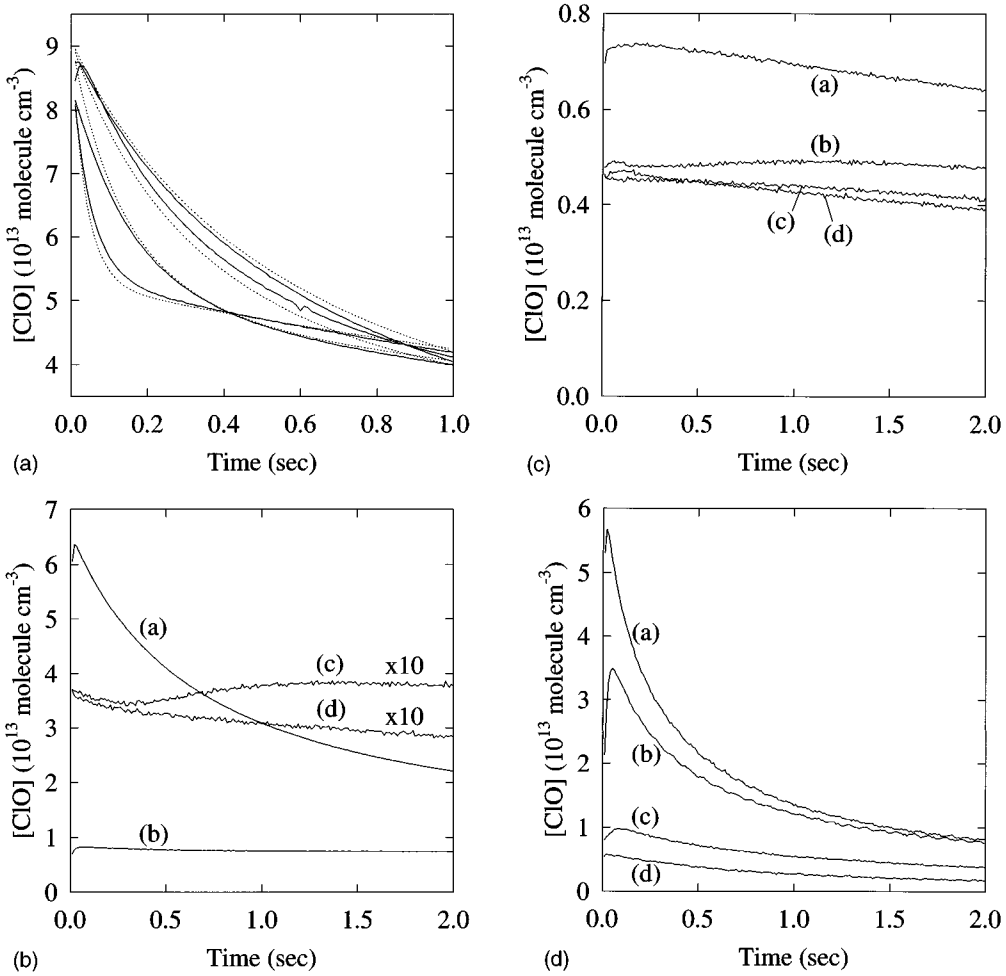

FIG. 3. (a) ClO temporal signals following Cl_2O photolysis in unfiltered quartz cell with N_2 bath gas at pressures of (a) 5.0 Torr; (b) 10.0 Torr; (c) 25.1 Torr; (d) 100.1 Torr. $[Cl_2O]_0=5\times10^{14}$ molecule cm^{-3}, $T=298$ K. Dotted lines indicate the fit of the data to a model which includes a single excited $Cl_2O^{\dagger}$ state undergoing competition between dissociation to products and quenching back to the ground state and the secondary chemistry of the ClO+ClO reactions. All four temporal signals were fit simultaneously with a single set of rate coefficients. (b) ClO temporal signals following Cl_2O photolysis in the quartz cell/$KMnO_4$ filter combination with N_2 bath gas at pressures of (a) 5.1 Torr; (b) 10.1 Torr; (c) 24.9 Torr; (d) 99.8 Torr. $[Cl_2O]_0=5\times10^{14}$ molecule cm^{-3}, $T=298$ K. (c) ClO temporal signals following Cl_2O photolysis in the quartz cell/$CrK(SO_4)_2\cdot12H_2O$ filter combination with N_2 bath gas at pressures of (a) 5.1 Torr; (b) 10.1 Torr; (c) 25.0 Torr; (d) 100.2 Torr. $[Cl_2O]_0=5\times10^{14}$ molecule cm^{-3}, $T=298$ K. (d) ClO temporal signals following Cl_2O photolysis in unfiltered Pyrex cell with N_2 bath gas at pressures of (a) 5.0 Torr; (b) 10.0 Torr; (c) 25.1 Torr; (d) 100.1 Torr. $[Cl_2O]_0=1\times10^{15}$ molecule cm^{-3}, $T=253$ K.

ditions of the transient signal. To further improve the signal-to-noise ratio of the spectrum, ten successive scans immediately preceding the flash were averaged to produce the baseline I_0 spectrum. The transient transmission spectrum, I_t, was obtained by averaging the first ten scans immediately following the flash. An absorption spectrum of the transient species was derived from the logarithm of the ratio of I_0 to I_t. By performing the additional averaging, the S/N is significantly improved, but the temporal resolution suffers accordingly. Each scan of the diode array requires 16.67 ms, so the overall temporal resolution is 167 ms.

Because the spectral bandwidth of the monochromator equipped with a 1200 line mm^{-1} grating was only 60 nm, to produce a complete absorption spectrum it was necessary to repeat the acquisition process at a number of monochromator settings spaced 30 nm apart beginning at 300 nm and extending to 580 nm. In this manner, the overlap between successive data sets was sufficient to allow accurate splicing of the individual spectra into a complete absorption spectrum covering this entire spectral region. Wavelength calibration of the spectrometer was accomplished by recording the emission lines from a mercury pen lamp with the diode array for each monochromator setting. This provided absolute wavelength markers throughout the entire region of the transient absorption spectra.

III. RESULTS

A. ClO formation and removal

Cl_2O photolysis experiments were conducted to determine the effects of (a) the spectral distribution of the photolysis radiation and (b) the identity and total pressure of buffer gas on the time-dependent formation and removal of ClO. Time-dependent ClO concentrations as a function of total pressure of N_2 are shown in Figs. 3(a)–3(d) for the four flashlamp spectral distributions. These signals were recorded

TABLE I. Summary of experimental results as a function of photolysis cell configuration and bath gas identity and density. $[ClO]_{max}$ is the concentration of ClO at the point of maximum signal, and t_{max} is the corresponding reaction time. Yield is defined as $[ClO]_{max}/[Cl_2O]_0$.

Cell configuration/ Bath gas	Pressure (Torr)	$[ClO]_{max}$ (10^{13} molecule cm^{-1})	t_{max} (s)	Yield
Quartz	5.0	8.76	0.02	0.175
N_2 bath gas	10.0	8.69	0.03	0.174
	15.0	8.29	0.02	0.166
	25.1	8.15	<0.01	0.163
	100.0	8.07	<0.01	0.161
Quartz/$KMnO_4$ filter	5.1	6.36	0.02	0.127
N_2 bath gas	10.1	0.824	0.07	0.016 5
	14.9	0.466	2.3	0.009 32
	25.0	0.383	1.4	0.007 66
	100.1	0.360	<0.01	0.007 20
Quartz/$CrK(SO_4)_2$ filter	5.1	0.735	0.20	0.014 7
N_2 bath gas	10.1	0.492	1.20	0.009 84
	15.3	0.488	0.08	0.009 76
	25.0	0.470	0.11	0.009 40
	100.2	0.460	<0.01	0.009 20
Pyrex/no filter	5.0	5.67	0.02	0.056 7
N_2 bath gas	10.0	3.50	0.05	0.035 0
	15.2	2.44	0.09	0.024 4
	25.1	0.971	0.10	0.009 71
	50.1	0.697	0.01	0.006 97
	100.1	0.553	0.02	0.005 53
Pyrex/no filter	5.0	3.42	0.024	0.101
O_2 bath gas	10.2	3.63	0.060	0.107
	15.2	2.70	0.084	0.079 4
	20.3	1.02	0.18	0.030 0
	30.4	0.613	0.27	0.018 0
	50.4	0.445	0.31	0.013 1
	100.3	0.209	0.41	0.006 15
	200.7	0.191	<0.004	0.005 62
	400.5	0.185	<0.004	0.005 44
Pyrex	5.1	1.75	<0.004	0.051 5
He bath gas	10.2	1.65	0.032	0.048 5
	15.3	1.57	0.044	0.046 2
	20.6	1.57	0.052	0.046 2
	30.4	1.42	0.096	0.041 8
	50.2	1.26	0.11	0.037 1
	100.3	0.774	0.24	0.022 8
	200.6	0.504	0.57	0.014 8
	400.5	0.331	0.55	0.009 74
Pyrex	5.3	1.51	0.24	0.044 4
SF_6 bath gas	10.1	1.57	0.21	0.046 2
	15.3	0.835	0.36	0.024 6
	20.5	0.661	0.44	0.019 4
	30.6	0.416	0.51	0.012 2
	50.5	0.297	0.46	0.008 74
	100.5	0.194	0.51	0.008 71

with a time resolution of 5 ms. In all cases, two processes contribute to the formation of ClO: direct photolysis of Cl_2O and the secondary reaction of atomic chlorine with Cl_2O. The initial rise of the signal due to the $Cl+Cl_2O \rightarrow ClO+Cl_2$ reaction is not seen because of the relatively long temporal resolution of the OMA. Experiments were carried out using Cl_2O concentrations in the range $(3–10)\times10^{14}$ molecule cm^{-3} and pressure range (5–400) Torr of buffer gas. Cl_2O concentrations were kept at a minimum to avoid possible effects of Cl_2O self-quenching. Most experiments were carried out at 298 K although a few were conducted at 253 K.

For photolysis in the quartz cell [Fig. 3(a)], the maximum ClO signal is essentially independent of the total pressure within the reaction cell. The decay of the signal is governed entirely by the self-reactions of ClO and can be modeled satisfactorily using the known rate coefficients for these reactions coupled with the flow of products from the cell (see Sec. IV). The time scale for ClO removal decreases with increasing pressure due to the termolecular component of the ClO self-reaction. The ClO yield, defined as the maximum ClO concentration normalized by the initial concentration of Cl_2O, is presented in Table I with other experimental parameters. For photolysis in the unfiltered quartz cell, the

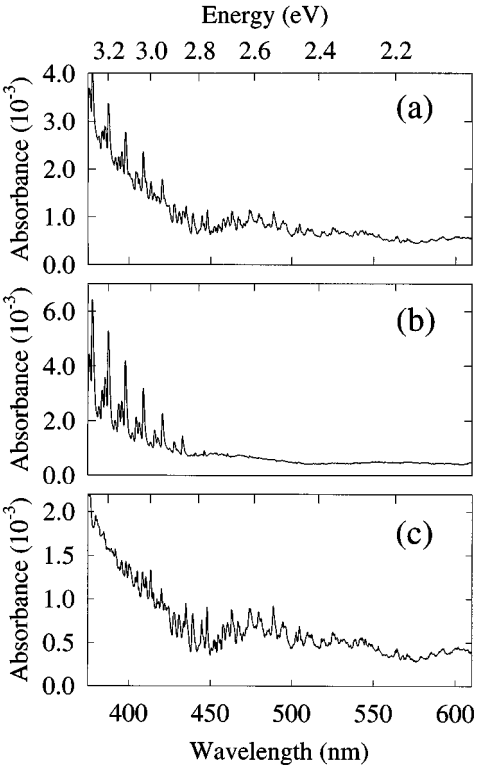

FIG. 4. (a) Total absorption spectrum collected from the first ten scans of the diode array immediately following firing of the flashlamp. $[Cl_2O]_0=1\times10^{15}$ molecule cm^{-3}, cell temperature was 253 K, and total pressure was 5.0 Torr with N_2 as the bath gas. (b) OClO absorption spectrum collected approximately 7 s following firing of the flashlamp when [OClO] is near its maximum. OClO is a product of the ClO+ClO reaction. (c) Cl_2O metastable intermediate absorption spectrum determined by subtracting an appropriately scaled OClO spectrum [Fig. 8(b)] from the total absorption spectrum [Fig. 8(a)].

yield is essentially constant over the density range $(1–30)\times10^{17}$ molecule cm^{-3}, and the time to the maximum signal becomes shorter with increasing pressure.

Figures 3(b) and 3(c) show ClO data collected using the quartz cell with the $KMnO_4$ and $CrK(SO_4)_2\cdot12H_2O$ filter solutions, respectively. Yield data are given in Table I. There is a marked difference when compared to the unfiltered quartz data of Fig. 3(a). For each experimental configuration, the data as a function of pressure display two prominent features. First, the ClO yield, as defined above, decreases with increasing bath gas density, and second, the time required to reach the maximum ClO signal increases as the bath gas density increases. Photolysis in the unfiltered quartz cell accesses both the strong absorption band of Cl_2O at 254 nm as well as the shoulder of the strong absorption feature in the region 200 to 225 nm (see Fig. 1). Photolysis using the filter solutions completely removes any contribution from the 200 to 225 nm band. The $KMnO_4$ filter severely limits the contribution from the 254 nm band, and the $CrK(SO_4)_2$ filter eliminates this contribution altogether. The difference in the product yield behavior between the unfiltered quartz cell and these filtered configurations can be related to the differences in the regions of the absorption spectrum accessed by the photolysis radiation.

TABLE II. MRCISD/cc-pVTZ total energies (hartree) and vertical excitation energies (eV) for singlet and triplet states of Cl_2O, calculated at the experimental ground-state geometry with CASSCF (14 in 9) state-averaged orbitals for pairs of states with the same space and spin symmetry.

State	E_{tot}(hartree)	E_{rel}	State	E_{tot}(hartree)	E_{rel}
$1\,^1A_1$	−994.365 50	0.0	$1\,^3B_1$	−994.269 04	2.625
$1\,^1B_1$	−994.240 30	3.407	$1\,^3A_2$	−994.217 88	4.017
$1\,^1A_2$	−994.183 42	4.954	$1\,^3B_2$	−994.212 55	4.162
$1\,^1B_2$	−994.182 33	4.984	$1\,^3A_1$	−994.204 31	4.386
$2\,^1A_1$	−994.165 09	5.453	$2\,^3A_2$	−994.158 97	5.620
$2\,^1A_2$	−994.150 88	5.840	$2\,^3A_1$	−994.130 17	6.404
$2\,^1B_1$	−994.096 75	7.313	$2\,^3B_2$	−994.124 75	6.552
$2\,^1B_2$	−994.073 60	7.943	$2\,^3B_1$	−994.120 43	6.669

Figure 3(d) shows the ClO temporal signals for photolysis in the Pyrex cell. The behavior is similar to that observed for the filtered quartz cell data, namely, that the yield decreases and the formation time to the maximum ClO signal increases as the bath gas density increases (see Table I). Use of the Pyrex cell limits the photolysis wavelengths to 300 nm thereby accessing only the ''weak'' transition on the shoulder of the 254 nm band and the bands at 410 and 530 nm. A series of measurements were also made using the Pyrex cell in which the temporal ClO behavior was monitored using either He, O_2, or SF_6 as the bath gas. The results are summarized in Table I. In each case, the yield decreased and the observed product formation time increased with increasing bath gas pressure. The effect of increased pressure on the experimental observables of yield and product formation time was more gradual with He as the bath gas, and was most pronounced with SF_6. For both O_2 and SF_6, the yield actually increased when the pressure was varied from 5 to 10 Torr, but then dropped rapidly at higher pressures.

Experiments were conducted to determine if the pressure-dependent ClO yields and temporal variations observed in the Pyrex cell were due to experimental artifacts peculiar to the cell material. A Pyrex sleeve was placed inside the quartz cell and the experiments were repeated. The results were identical with those obtained in the Pyrex cell ruling out an artifacts associated with the cell itself (other than the cell material). Another test was made in which an opaque liner was placed inside the Pyrex cell to block the photolysis light from entering. The observed formation of ClO was negligible indicating that the dissociation of Cl_2O occurred by photolysis rather than some other process such as some sort of electrostatic discharge arising from the high voltage pulse on the xenon flash lamp.

B. Metastable intermediate formation

The dependence of the ClO yield on the buffer gas density suggests that in addition to a direct dissociation pathway, a metastable intermediate is formed which subsequently decomposes to ClO or quenches to one or more other states. Using the OMA, a spectral search was carried out for transient absorbers to identify other species or metastable states which might be formed from the photolysis. Based on simulations of the secondary chemistry of the species expected to

TABLE III. MRCISD/cc-pVTZ vertical excitation energies (eV) and oscillator strengths for singlet states (relative to S_0) and triplet states (relative to T_0)[a] calculated at the experimental ground-state geometry for Cl_2O with three-state CASSCF (14 in 9) averaged orbitals.

State	E_{rel}	f	State	E_{rel}	f
$1\,^1A_1$	0.0		$1\,^3B_1$[a]	0.0	
$1\,^1B_1$	3.419	1.42×10^{-4}	$1\,^3A_2$	1.417	8.81×10^{-4}
$1\,^1A_2$	4.969	0.0	$1\,^3B_2$	1.559	0.0
$1\,^1B_2$	4.983	7.75×10^{-3}	$1\,^3A_1$	1.775	3.3×10^{-6}
$2\,^1A_1$	5.453	8.5×10^{-5}	$2\,^3A_2$	3.009	1.03×10^{-1}
$2\,^1A_2$	5.884	0.0	$2\,^3A_1$	3.819	8.0×10^{-5}
$2\,^1B_1$	7.345	5.26×10^{-3}	$2\,^3B_2$	3.962	0.0
$2\,^1B_2$	7.981	6.0×10^{-6}	$2\,^3B_1$	4.044	5.37×10^{-3}

[a]$T_0(1\,^3B_1)$ state is 2.625 eV above $S_0(1\,^1A_1)$.

be present in the cell following the flash, the only species with absorptions in the region 350 to 550 nm are Cl_2O itself, and OClO and Cl_2 which are products of the ClO self-reaction. The absorption spectrum of ground state Cl_2O is broad with no sharp distinguishing features and will result only in gradual variations of the baseline. Similarly, the Cl_2 spectrum is a broad continuum and will produce no sharp features in the absorption spectrum. OClO has a structured spectrum from 270 to 475 nm corresponding to a vibrational progression in the $A\leftarrow X$ band. To remove the OClO contribution to the product spectrum, a reference spectrum was produced from the OMA data collected at times greater than 7.5 s following the flash when the reactions which result in OClO production were essentially complete. The OClO reference spectrum was appropriately scaled and subtracted from the total absorption spectrum. Figures 4(a)–4(c) displays three spectra: (a) the total absorption spectrum for all species immediately following the flash, (b) the OClO reference spectrum, and (c) the spectrum resulting from the removal of the OClO contribution. Figure 4(c) shows a weak absorption spectrum with a complex series of vibrational progressions over the spectral range 400–600 nm. The temporal dependence of the residual spectrum was measured and found to persist for about 500 ms. The absorption spectrum of the metastable maximized at low pressure (5 Torr N_2 at a temperature of 253 K).

The spectrum of Fig. 4(c) cannot be assigned to any of the other species that might be produced from secondary reactions of Cl_2O photolysis products (ClOO, ClO_3, Cl_2O_2, etc.) or from minor impurities in the Cl_2O. The structured bands are well above the noise level of the data and were reproduced a number of times using Cl_2O samples prepared at different times. In addition, all of the absorption bands in the new spectrum showed the same time dependence indicating the presence of a single absorber. The increase in baseline absorption at shorter wavelengths is attributed to changes in the concentration of ground state Cl_2O; the Cl_2O spectrum was not subtracted out because the broad absorption bands of ground state Cl_2O do not interfere with the structured spectrum of the intermediate.

IV. DISCUSSION

The interpretation of the results of this work is heavily reliant upon an understanding of the energetics and symmetry properties of the Cl_2O excited states. We begin by discussing the methods and results of the *ab initio* calculations, then use these results to interpret the ClO formation kinetics and the spectrum of the observed metastable intermediate.

A. Computational methods

Theoretical calculations for excited states of Cl_2O were carried out using MOLPRO,[14] a set of *ab initio* electronic structure programs. Complete-active-space self-consistent-field (CASSCF)[15] calculations were performed for the two states of lowest energy within each irreducible representation of the C_{2v} point group, for both the singlet and triplet manifolds, using the experimentally determined ground-state molecular geometry. Subsequently the CASSCF molecular orbitals (MOs) were used in multireference configuration-interaction (MRCI) calculations for these states.[16] These were of the internally contracted type, and used the projection method of Knowles and Werner.[17]

The Hartree–Fock electronic configuration for the $X\,^1A_1$ ground state of Cl_2O is $(\text{core})(6a_1)^2(5b_2)^2(7a_1)^2(2b_1)^2(6b_2)^2(8a_1)^2(2a_2)^2(9a_1)^2(7b_2)^2(3b_1)^2(8b_2)^0(10a_1)^0$, where the $9a_1$ and $6b_2$ MOs are ClO σ bonding and the unoccupied $8b_2$ and $10a_1$ MOs are ClO σ antibonding. The active space for full-valence CASSCF calculations would comprise all these MOs, giving 20 electrons in 12 orbitals. Inspection of the CASSCF CI vectors for this active space showed that, for all the states calculated, the MOs $6a_1$, $7a_1$, and $5b_2$, (arising from the Cl $3s$ and O $2s$ orbitals) remained doubly occupied in all significant configurations. By excluding these three MOs the active space was reduced to 14 electrons in 9 orbitals, arising from the valence p subshell of each atom. A total of between 158 and 167 configuration state functions (CSFs) were generated from this active space for the various states calculated. Further examination of the CASSCF CI vectors showed that for all symmetry species the predominant configurations had at least two electrons in the orbitals $8a_1$ and $6b_2$. The final reference space adopted for the MRCI calculations therefore comprised all the CASSCF CSFs except those in which the combined occupancy of the $8a_1$ and $6b_2$ was less than two; elimination of these configurations had only a minor effect on the total number of CSFs.

The calculations were performed using the Dunning correlation-consistent polarized valence triple-zeta (cc-pVTZ) basis,[18] which has the form $(10s5p2d1f)/[4s3p2d1f]$ for oxygen and $(15s9p2d1f)/[5s4p2d1f]$ for chlorine; this gave a total number of 98 basis functions. To check for basis-set effects in the results, calculations were also made with a smaller valence double-zeta basis (involving only 50 basis functions) but the results were found to differ very little.

B. Computational results and discussion

Table II shows total energies and vertical transition energies, calculated at the MRCISD/cc-pVTZ level, for the fol-

lowing excited states: $1\,^1A_1$, $2\,^1A_1$, $1\,^1B_1$, $2\,^1B_1$, $1\,^1B_2$, $2\,^1B_2$, $1\,^1A_2$, $2\,^1A_2$, $1\,^3A_1$, $2\,^3A_1$, $1\,^3B_1$, $2\,^3B_1$, $1\,^3B_2$, $1\,^3B_2$, $1\,^3A_2$, and $2\,^3A_2$. State-averaged orbitals were used for each of the different space and spin symmetries in order to avoid bias towards the lower energy states. First, eight separate two-state CASSCF (14 in 9) calculations were performed for $(X\,^1A_1+2\,^1A_1)$, $(1\,^1B_1+2\,^1B_1)$, $(1\,^1B_2+2\,^1B_2)$, $(1\,^1A_2+2\,^1A_2)$, $(1\,^3A_1+2\,^3A_1)$, $(1\,^3B_1+2\,^3B_1)$, $(1\,^3B_2+2\,^3B_2)$, and $(1\,^3A_2+2\,^3A_2)$. The MOs from each of these calculations were then used in MRCISD calculations for the two states; e.g., the MOs from the $(1\,^1B_2+2\,^1B_2)$ CASSCF calculation were used to calculate the energies of the first and second $^1B_2$ states at the MRCISD level.

Transition dipole moments (and hence oscillator strengths) between the lowest-energy state and each higher state, within both the singlet and triplet manifolds, were calculated at the MRCISD/cc-pVTZ level, as shown in Table III. It is necessary to employ the same orbitals for both states involved in each transition.[19] Thus to obtain orbitals averaged over both the lower and upper state required a further three-state CASSCF (14 in 9) calculation, i.e., $(X\,^1A_1+1\,^1B_1+2\,^1B_1)$, $(X\,^1A_1+1\,^1B_2+2\,^1B_2)$, $(X\,^1A_1+1\,^1A_2+2\,^1A_2)$, $(1\,^3B_1+1\,^3A_1+2\,^3A_1)$, $(1\,^3B_1+1\,^3B_2+2\,^3B_2)$, and $(1\,^3B_1+1\,^3A_2+2\,^3A_2)$, unless the upper and lower states were already of the same symmetry. To calculate the transition dipole moment for the transition $(2\,^3A_2\leftarrow 1\,^3B_1)$, for example, an MRCISD wave function for each state was determined using the orbitals from the $(1\,^3B_1+1\,^3A_2+2\,^3A_2)$ calculation. Since the three-state CASSCF calculations give orbitals that are less well adapted to each individual state than are those from the two-state CASSCF calculations, the resulting energies are slightly less satisfactory for each state. However, comparison of the transition energies in Tables II and III reveals no significant differences. Moreover, it was found that very similar results were obtained for transition energies and oscillator strengths at the CASSCF level using either the (14 in 9) or the larger (20 in 12) active space, and with either the cc-pVTZ or the smaller cc-pVDZ basis; these findings (not shown) confirm the essential reliability of the results presented.

The lowest energy triplet state calculated was $1\,^3B_1$. The predominant configuration in the MRCISD vector for this state corresponds to an excitation from the $(3b_1)^2$ nonbonding orbital of the Hartree–Fock ground state to the $(10a_1)^0\sigma^*$(ClO) antibonding orbital. The transition with the largest oscillator strength is $2\,^3A_2\leftarrow 1\,^3B_1$; this transition corresponds to excitation of an electron from the doubly occupied $(2a_2)^2$ orbital in the $1\,^3B_1$ state to the singly occupied $(3b_1)^1$ orbital.

The computed vertical excitation energies and oscillator strengths of Table III may be used to interpret the observed Cl_2O absorption spectrum shown in Fig. 1. The experimental spectrum has five prominent features in the region of interest to this study—absorption peaks at 171 nm (7.24 eV), 254 nm (4.88 eV), 420 nm (2.9 eV), and 540 nm (2.3 eV), and a shoulder on the 254 nm peak at 300 nm (4.1 eV). The largest peak at 7.24 eV correlates well with the calculated energy of 7.345 eV for the $2\,^1B_1$ state. The peak observed at 4.88 eV is consistent with the $1\,^1B_2$ state calculated to be at 4.983 eV. Examination of the computed oscillator strengths indicates that these two states should indeed have the strongest absorptions in agreement with the observed spectrum. However, the ordering is reversed—*ab initio* results predict the $1\,^1B_2$ state to have a slightly larger absorption cross section relative to the $2\,^1B_1$ state whereas the experimental spectrum indicates a larger oscillator strength for the higher energy state.

The computed oscillator strengths indicate that the next strongest absorption following the two large features is the transition to the $1\,^1B_1$ state. The calculated energy of this transition is 3.419 eV which does not directly correlate with any features of the observed absorption spectrum. However, the shoulder to the low energy side of the 254 nm peak is of sufficient strength that this feature most likely arises from the $1\,^1B_1\leftarrow 1\,^1A_1$ transition. If this is indeed the case, then the calculated transition energy of this state is low by several tenths of an eV. The transition to the $2\,^1A_1$ state at 5.453 eV also has sufficient oscillator strength to be observed experimentally, but this absorption is buried in the shoulder of the large feature at 7.24 eV.

The weak absorption peaks at 2.3 and 2.9 eV cannot be assigned to singlet←singlet transitions because the $1\,^1B_1$ state is the lowest excited state in the singlet manifold, and the energy of this state is substantially higher than the observed transition energies of these two features. The 2.9 eV peak corresponds to a spin forbidden transition to the lowest lying triplet state, $1\,^3B_1$. The oscillator strength for this triplet←singlet transition was not determined in this study, but this assignment is consistent with the calculated transition energy of 2.625 eV and the small absorption cross section of 1×10^{-20} cm^2 expected for a forbidden transition such as this. However, that excitation of this triplet state occurs is an indication that the $1\,^3B_1$ state is not strictly triplet in nature, but rather has a mixed configuration containing some singlet character. The very weak feature at 2.3 eV cannot be assigned to a transition from the ground electronic state since the excitation energy is significantly lower than any of the calculated excited state energies in either the singlet or triplet manifolds. This absorption may arise from a transition between two excited electronic states where the lower lying state is prepared by excitation from the ground state.

C. ClO formation kinetics

Our experiments focused on the production of ClO from the broadband pulsed photolysis of Cl_2O using different photolytic spectral distributions extending from the visible to 200 nm. The ClO time dependence was dominated by two major effects: The kinetics of ClO formation which, when photolyzed at longer wavelengths, were determined primarily by the excited state dynamics of Cl_2O and the kinetics of ClO removal which were dominated by ClO self-reaction. These processes will be discussed below.

The time dependence of ClO production was influenced strongly by the spectral domain of the photolysis radiation, the bath gas pressure and the bath gas identity. Restricting

the spectrum of the photolysis radiation to wavelengths longer than about 250 nm results in significant changes in the production of ClO. First, the time scale for the formation of ClO ($X\ ^2\Pi$) changes from instantaneous on the scale of the OMA temporal resolution to values in the range of 50–200 ms. The time at which the ClO maximum is reached increases with increasing bath gas density until about 100 Torr at which point the time to reach the maximum decreased. Second, the maximum photolytic yield of ClO changes from being independent of the bath gas density to inversely dependent on the density. These observations strongly suggest that Cl_2O photolysis beyond 250 nm results in the formation of metastable states which undergo competitive collisional deactivation and unimolecular decomposition to form ClO and possibly other products. Due to the broadband nature of the photolysis spectrum, the wavelength dependence of the excitation leading to the Cl_2O metastable cannot be determined. The observed behavior is a convolution of the photolytic intensity distribution which increases rapidly at longer wavelengths, the absorption cross sections which decrease rapidly at longer wavelengths, and the energy dependence of the excitation leading to the curve crossing which is unknown.

Insight into the excited state dynamics arising from the long-wavelength excitation may be obtained from a kinetic simulation of the ClO temporal profile and its dependence on the buffer gas density. The simplest mechanism for the formation of ClO product consists of a single metastable excited state with competition between quenching and dissociation, i.e.,

$$Cl_2O + h\nu \rightarrow Cl_2O^{\dagger} \quad \text{excitation},$$

$$Cl_2O^{\dagger} \xrightarrow{k_d} ClO + Cl \quad \text{dissociation},$$

$$Cl_2O^{\dagger} + M \xrightarrow{k_q} Cl_2O + M \quad \text{quenching}.$$

The time dependence for ClO formation is given by

$$[ClO] = \frac{k_d[Cl_2O^{\dagger}]_0}{k_d + k_q[M]} (1 - e^{-(k_d + k_q[M])t}).$$

The kinetics of the ClO removal are dominated by the self-reaction of ClO. As discussed by Nickolaisen *et al.*,[13] the detailed mechanism of the ClO self-reaction consists of both bimolecular and termolecular components at temperatures above about 250 K. The detailed reaction mechanism is given in Table IV. The time scale for ClO removal by ClO self-reaction is sufficiently long ($t > 0.1$ s) that the ClO removal mechanism can be decoupled from the excited state dynamics which produce ClO at long wavelengths. This mechanism for ClO formation coupled with the ClO self-reaction kinetics predicts that as the pressure is increased, the time to reach the maximum ClO signal will decrease. The observed ClO signals for photolysis in the unfiltered quartz cell conform to the time dependence predicted by this equation. Figure 3(a) illustrates the fit of the unfiltered quartz cell data to a mechanism that included the above elementary steps and all chemical processes involved in the ClO self-reaction. Reactions and rate coefficients for the ClO removal processes are given in Table IV. The simulations were performed by simultaneously fitting the ClO time dependent signals at pressures of 5, 10, 25, and 100 Torr to this mechanism using a nonlinear least-squares technique. The parameters varied in the fitting routine were the initial amount of $[Cl_2O^{\dagger}]_0$, k_d, and k_q. The resulting values were $[Cl_2O^{\dagger}]_0 = 5.4\times10^{13}$ molecule cm^{-3}, $k_d = 1.5\times10^{13}$ s^{-1}, and $k_q = 4.4\times10^{-14}$ cm^3 molecule^{-1} s^{-1}. The values for k_d and k_q are reasonable, but may not accurately represent the rate coefficients for these physical processes because the hypersurface used in the fitting routine is not tightly constrained by the data.

TABLE IV. Mechanism for the simulation of ClO kinetic decay in the photolysis of Cl_2O.

Reaction	k (cm^3 molecule^{-1} s^{-1})	Reference
$Cl_2O + h\nu \rightarrow ClO + Cl$	$\Phi = 0.75$	5
$Cl_2O + h\nu \rightarrow Cl_2 + O$	$\Phi = 0.25$	5
$Cl_2O + Cl \rightarrow ClO + Cl_2$	9.8×10^{-11}	20
$Cl_2O + O \rightarrow 2ClO$	3.5×10^{-12}	20
$ClO + ClO \rightarrow Cl_2 + O_2$	4.9×10^{-15}	13
$ClO + ClO \rightarrow ClOO + Cl$	8.0×10^{-15}	13
$ClO + ClO \rightarrow OClO + Cl$	3.5×10^{-15}	13
$ClO + ClO + M \rightarrow Cl_2O_2 + M$	$(0.99-3.15)\times10^{-32}$[a]	13
$O + ClO \rightarrow Cl + O_2$	3.8×10^{-11}	20
$O + OClO \rightarrow ClO + O_2$	1.0×10^{-13}	20
$Cl + ClOO \rightarrow 2ClO$	1.2×10^{-11}	20
$Cl + ClOO \rightarrow Cl_2 + O_2$	2.3×10^{-10}	20
$Cl + Cl_2O_2 \rightarrow ClOO + Cl_2$	1.0×10^{-10}	20
$ClOO + M \rightarrow Cl + O_2 + M$	1.1×10^{-12}	20
$Cl_2O_2 + M \rightarrow 2ClO + M$	2.3×10^{-18}	20
$Cl + O_2 + M \rightarrow ClOO + M$	2.7×10^{-33}[a]	20
$O + OClO + M \rightarrow ClO_3 + M$	1.9×10^{-31}[a]	21

[a]Units are cm^6 molecule^{-2} s^{-1}.

While this mechanism predicts the ClO yield and temporal behavior for photolysis at short wavelengths, it does not describe the experimental data for the other photolysis configurations in which absorption to the $2\ ^1B_1$ state is not involved. To model the temporal behavior correctly, it was necessary to include two excited states in the mechanism. The first state is populated either directly by photolysis or by intersystem crossing from the initially prepared singlet upper state. The second state is produced by collisional relaxation from the first state and may dissociate to products or undergo collisional quenching to the ground state. Examination of the energy level diagram in Fig. 5 suggests that plausible candidates for the two metastable excited states are the $1\ ^3A_2$ and $1\ ^3B_1$ states, respectively, and that the initially prepared singlet state in this wavelength region is $1\ ^1B_1$. The complete mechanism is

$$Cl_2O(1\ ^1A_1) + h\nu \rightarrow Cl_2O(1\ ^1B_1),$$

$$Cl_2O(1\ ^1B_1) \rightarrow Cl_2O(1\ ^3A_2),$$

$$Cl_2O(1\ ^3A_2) \rightarrow ClO + Cl,$$

$$Cl_2O(1\ ^3A_2) + M \rightarrow Cl_2O(1\ ^3B_1) + M,$$

$$Cl_2O(1\ ^3B_1) \rightarrow ClO + Cl,$$

$$Cl_2O(1\ ^3B_1) + M \rightarrow Cl_2O(1\ ^1A_1) + M.$$

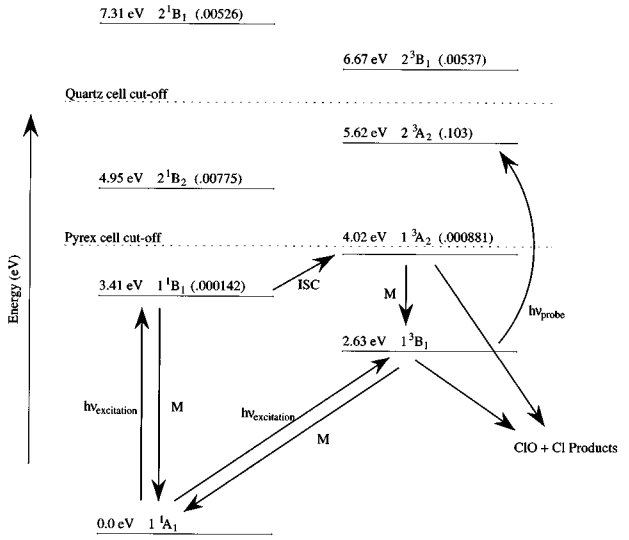

FIG. 5. Energy diagram of Cl_2O electronic states. Vertical excitation energies are given in eV, and oscillator strengths are included in parentheses for each state. Bold lines indicate processes involved in the long wavelength photolysis. $h\nu_{excitation}$ represents excitation by the xenon flashlamp, *M* indicates collisional quenching, ISC indicates intersystem crossing, and $h\nu_{probe}$ represents absorption to produce the observed metastable spectrum.

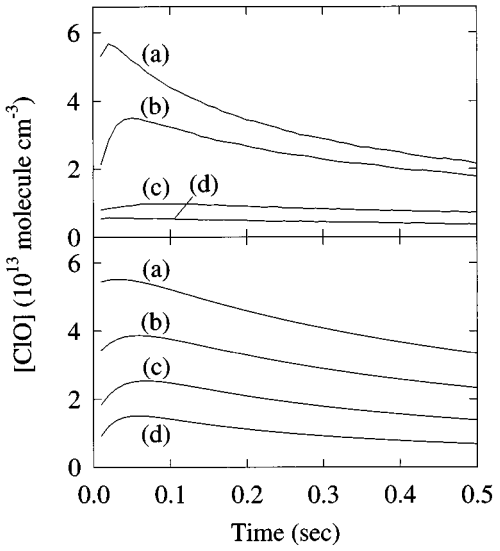

FIG. 6. ClO temporal signals resulting from model simulations of the reaction mechanism which includes quenching to a Cl_2O metastable intermediate from the initially excited electronic state, dissociation of the intermediate state, and quenching of the intermediate state to the ground state. Upper panel is the experimental data of Figure 3(d) with an expanded time axis. Lower panel are the simulated data. Total pressures are (a) 5 Torr; (b) 10 Torr; (c) 25 Torr; (d) 100 Torr.

Figure 5 schematically indicates the process occurring during Cl_2O photolysis for wavelengths greater than 300 nm. Initial excitation from the ground state is dominated by transition to the $1\,^1B_1$ state with a small fraction (from the relative absorption cross sections, perhaps 1%–2%) of population in the $1\,^3B_1$ state. As mentioned previously, the actual energy of the $1\,^1B_1$ state is higher than shown in Fig. 5, and is probably much closer to the wavelength cut off of the Pyrex cell at 300 nm. Thus the $1\,^1B_1$ and $1\,^3A_2$ states will be in near resonance so that intersystem crossing to the triplet manifold from the initially prepared singlet state occurs. This process is very efficient because of the energy overlap of rovibrational levels within the $1\,^1B_1$ and $1\,^3A_2$ states, the density of rovibrational states, and the probable mixed character of the $1\,^3A_2$ state. As a result, the $1\,^1B_1$ state undergoes competition between intersystem crossing to the $1\,^3A_2$ state and collisional quenching to the ground state.

Once in the triplet manifold, $Cl_2O(1\,^3A_2)$ either dissociates to products or is collisionally quenched to the lowest lying $1\,^3B_1$ state. The $1\,^3B_1$ state, in turn, may also dissociate to products or be quenched to the ground $1\,^1A_1$ state. The quenching step is quite inefficient because of the spin forbidden nature of the transition and the large energy difference between states, so that this process becomes significant only at higher pressures. We know that the lifetime of the $1\,^3B_1$ state is quite long because it is this state that is the source of the intermediate absorption spectrum measured in these experiments. Hence, the dissociation process from this lowest triplet state must also be inefficient. This mechanism was used to simulate the ClO temporal signals of Fig. 3(d) for photolysis in the Pyrex cell at 253 K with nitrogen as the bath gas over the pressure range 5–100 Torr. Results are shown in Fig. 6. The qualitative features of the experimental data are reproduced by this mechanism, namely, that the ClO yield decreases and the time required to attain the maximum ClO signal initially increases and then decreases with increasing bath gas density. The model could not be made to fit the data quantitatively. This is due to the simplified nature of the excited state mechanism and the computational difficulties involved in deriving a best fit of four data sets to a six-parameter mechanism.

The transient absorption spectrum shown in Fig. 4(c) is important in the interpretation of the dissociation mechanism. As mentioned previously, the transient spectrum is highly structured and cannot be attributed to any of the known transient radical or stable molecular species produced chemically in the above mechanism. A possible explanation is that the transient spectrum arises from the formation of a $ClO\cdot Cl_2O$ complex since, immediately following the photolysis pulse, the reaction cell contains relatively high concentrations of both ClO and Cl_2O. If adduct formation was the source of the observed transient spectrum, the adduct would also be seen in the quartz cell in even higher concentrations because more ClO is produced under these photolysis conditions. However, careful examination of the data following quartz cell photolysis provided no evidence of the transient spectrum seen in the Pyrex cell. Adduct formation also fails to describe the observed increase in the ClO product formation rate with increasing pressure. A $ClO\cdot Cl_2O$ complex would have the same kinetic behavior as a function of pressure as ClO dimer formation. Simulations of a mechanism that includes adduct formation indicate that the opposite effect on the product formation rate should be observed, namely, that the rate of product formation becomes faster

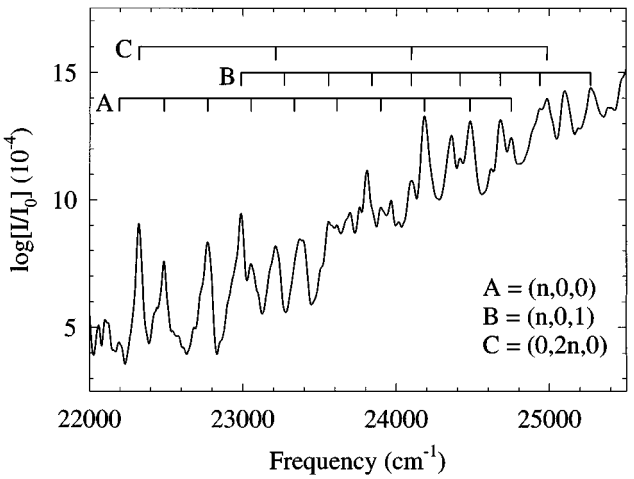

FIG. 7. Vibronic band assignments are shown for the dominant progressions of the metastable Cl_2O spectrum observed between 22 000 and 26 000 cm^{-1}. The long progressions *A* and *B* have frequencies characteristic of a Cl–O stretching mode and suggest significant differences between the T_0 and T_1 equilibrium structures.

with increased pressure. These two points argue against a $ClO \cdot Cl_2O$ complex as the source of the transient spectrum.

D. Spectral analysis

The spectrum of the transient absorber shown in Fig. 4(c) displays extensive, complicated vibronic structure. Closer inspection shows that the spectrum separates into three distinguishable sections. The lowest energy region (16 600–20 000 cm^{-1}) is characterized by a series of low intensity features with ~100 and ~300 cm^{-1} spacing, but lacking a well-defined origin. A positive identification of any regular progressions is complicated by the near resonance of 3×times 100 with 300 cm^{-1} and the fact that these bands overlap one another in most instances.

The intermediate energy region (20 000–22 000 cm^{-1}) has the type of overall intensity contour one would expect for a Franck–Condon envelope. The strength of individual features increases from a minimum near 20 000 cm^{-1}, peaks near 21 000 cm^{-1}, then slowly decreases with increasing energy. The number of features in this energy range, however, is far larger than one might expect for the spectrum of a well-behaved triatomic molecule. We have identified fragmentary series having 110, 325, and 768 cm^{-1} spacings in this region as well as a number of series having 345–350 cm^{-1} spacings but we have been unable to establish a unique origin for the bands in this region.

The spectrum changes significantly in the 22 000–26 000 cm^{-1} region. An expanded view of this region is shown in Fig. 7. The first few features in this region are quite intense and well separated from their neighbors. It was possible to identify progressions having 283, 443, and 505 cm^{-1} differences using the strong feature at 22 322 cm^{-1} as a starting point. Incorporating these three frequencies into an harmonic oscillator calculation, 31 features were fitted within the experimental resolution of the spectrum. The dominant progression was one with up to 8 quanta of excitation in the 283 cm^{-1} mode. This frequency is consistent with a ClOCl bending motion and indicates a significant change in the bond angle between the upper and lower electronic states. Another interesting aspect of the spectrum in this region is the presence of a strong progression at 886 cm^{-1}, which may indicate that 443 cm^{-1} corresponds to an antisymmetric ClO stretching motion. A more quantitative analysis of the spectrum requires higher resolution data.

The *ab initio* excitation energies and oscillator strengths given in Tables II and III for electronic transitions within the Cl_2O triplet manifold are consistent with the experimentally observed transient absorption spectrum. There are only two excited electronic states energetically accessible after Cl_2O photoexcitation with wavelengths longer than 350 nm: $1\,^1B_1$ (S_1; λ_{thresh}=364 nm) and $1\,^3B_1$ (T_0; λ_{thresh}=472 nm). While we cannot eliminate singlet–singlet transitions originating from S_1 as the source of the metastable spectrum, the $2\,^3A_2 \leftarrow 1\,^3B_1$ transition has an unusually large oscillator strength and is at least an order of magnitude stronger than any other singlet or triplet transition listed. Additionally, the calculated transition energy, ~3.0 eV (24 200 cm^{-1}), lies within the range of the experimentally observed transient spectrum. Our calculations are still exploratory at this stage and should not be used for definitive spectral assignments, but they do suggest that the upper state in the 22 000–26 000 cm^{-1} transition may possess a large fraction of $2\,^3A_2$ character.

The *ab initio* calculations also suggest an explanation for the complicated, low intensity features present below 22 000 cm^{-1}. Three excited triplet configurations were identified at energies below the $2\,^3A_2$ state. Any or all of these states could mix with the $2\,^3A_2$ state and borrow oscillator strength, thereby producing observable absorptions and complicated vibronic patterns. Similarly, mixing between the nearly degenerate $2\,^1A_2$ and $2\,^3A_2$ states might provide sufficient oscillator strength to produce some features in the otherwise forbidden $2\,^1A_2 \leftarrow 1\,^3B_1$ transition. Severe perturbations in the vibrational spacings of the spectrum might also result from mixing of the metastable eigenstates with the manifold of dark S_0 and/or T_0 levels. Further experimental and theoretical studies are required to uncover these aspects of Cl_2O photochemistry.

The observed pressure dependent photolysis yields for Cl_2O may have important implications for stratospheric chemistry. For most temporary reservoirs of odd hydrogen, nitrogen, chlorine and bromine in the lower stratosphere, photolysis is the dominant loss mechanism. Below about 26 km, photolysis is restricted to wavelengths longer than about 290 nm due to absorption by ozone at higher altitudes. Above this wavelength, absorption cross sections are generally less than 5×10^{-20} cm^2 $molecule^{-1}$, decreasing rapidly with wavelength. Excitations in this region may be dominated by weak transitions whose dissociation dynamics are highly uncertain because quantum yield studies typically address the more intense region of the continuum. Species that fall into this category include $ClONO_2$, N_2O_5, H_2O_2, HNO_3, and HO_2NO_2. Using the same technique employed for the Cl_2O studies, we have observed that the yields of ClO and

NO_3 from the photolysis of $ClONO_2$ at wavelengths longer than 300 nm are also pressure dependent.[22] In order to assess the importance of this mechanism for stratospheric chemistry it is necessary to carry out quantum yield studies using monochromatic excitation over a range of wavelengths and bath gas densities appropriate for the lower stratosphere.

ACKNOWLEDGMENTS

We wish to thank the JPL kinetics and photochemistry group, C. Wittig and H. Reisler for helpful discussions and R. Beaudet for his preliminary analysis of the metastable spectrum. Part of the research described in this paper was carried out at the Jet Propulsion Laboratory, California Institute of Technology, under contract to the National Aeronautics and Space Administration.

[1] W. Finkelnburg, H. J. Schumacher, and G. Stieger, Z. Phys. Chem. B **15**, 127 (1931).
[2] H. J. Schumacher and R. V. Townend, Z. Phys. Chem. B **20**, 375 (1933).
[3] F. H. C. Edgecomb, R. G. W. Norrish, and B. A. Thrush, Proc. R. Soc. London Ser. A **243**, 24 (1957).
[4] N. Basco and S. K. Dogra, Proc. R. Soc. London, Ser. A **323**, 401 (1971).
[5] S. P. Sander and R. R. Friedl, J. Phys. Chem. **93**, 4764 (1989).
[6] C. M. Nelson, T. A. Moore, and M. Okumura, J. Chem. Phys. **100**, 8055 (1994).
[7] A. I. Chichinin, Chem. Phys. Lett. **209**, 459 (1993).
[8] C.-L. Lin, J. Chem. Eng. Data **21**, 411 (1976).
[9] L. T. Molina and M. J. Molina, J. Phys. Chem. **82**, 2410 (1978).
[10] H. D. Knauth, H. Alberti, and H. Clausen, J. Phys. Chem. **83**, 1604 (1979).
[11] J. B. Nee, J. Quant. Spectrosc. Radiat. Transfer **46**, 55 (1991).
[12] G. H. Cady Inorg. Synth. **5**, 156 (1957).
[13] S. L. Nickolaisen, R. R. Friedl, and S. P. Sander, J. Phys. Chem. **98**, 155 (1994).
[14] MOLPRO: a package of *ab initio* programs written by H.-J. Werner and P. J. Knowles, with contributions of J. Almlof, R. Amos, S. Elbert, K. Hampel, W. Meyer, K. Peterson, R. Pitzer, and A. Stone.
[15] H.-J. Werner and P. J. Knowles, J. Chem. Phys. **82**, 5053 (1985); P. J. Knowles and H.-J. Werner, Chem. Phys. Lett. **115**, 259 (1985).
[16] H.-J. Werner and P. J. Knowles, J. Chem. Phys. **89**, 5803 (1988); P. J. Knowles and H.-J. Werner, Chem. Phys. Lett. **145**, 514 (1988).
[17] P. J. Knowles and H. J. Werner, Theor. Chim. Acta **84**, 95 (1988).
[18] T. H. Dunning, J. Chem. Phys. **90**, 1007 (1989); D. E. Woon and T. H. Dunning *ibid*. **98**, 1358 (1993).
[19] C. W. Bauschlicher, Jr. and S. R. Langhoff, Chem. Rev. **91**, 701 (1991).
[20] W. B. DeMore, S. P. Sander, D. M. Golden, R. F. Hampson, M. J. Kurylo, C. J. Howard, A. R. Ravishankara, C. E. Kolb, and M. J. Molina, *Chemical Kinetics and Photochemical Data for Use in Stratospheric Modeling—Evaluation Number 11*, JPL Publication 94-26, Jet Propulsion Laboratory, Pasadena (1994).
[21] A. J. Colussi, S. P. Sander, and R. R. Friedl, J. Phys. Chem. **96**, 4442 (1992).
[22] S. L. Nickolaisen, S. P. Sander, and R. R. Friedl, J. Phys. Chem. (submitted).